PHILOSOPHICAL TRANSACTIONS A

rsta.royalsocietypublishing.org

Research

Article submitted to journal

Subject Areas:
Rare event sampling, Markov Chain Monte Carlo (MCMC), Power systems engineering

Keywords:
Power system dynamics, Battery energy storage systems, CVaR.

Author for correspondence:
Maldon Patrice Goodridge
e-mail: m.p.goodridge@qmul.ac.uk

A rare-event study of frequency regulation and contingency services from grid-scale batteries

Maldon Patrice Goodridge[1] John Moriarty[1] and Andrea Pizzoferrato[2 3]

[1]Queen Mary University of London
[2]University of Bath
[3]The Alan Turing Institute, London

We perform a rare-event study on a simulated power system in which grid-scale batteries provide both regulation and emergency frequency control ancillary services. Using a model of random power disturbances at each bus, we employ the skipping sampler, a Markov Chain Monte Carlo algorithm for rare-event sampling, to build conditional distributions of the power disturbances leading to two kinds of instability: frequency excursions outside the normal operating band, and load shedding. Potential saturation in the benefits, and competition between the two services, are explored as the battery maximum power output increases.

THE ROYAL SOCIETY PUBLISHING

1. Introduction

A growing number of countries are transitioning their energy generation from fossil to renewable energy sources (RES), due to an increased desire to mitigate the effects of climate change [1]. While on one side this shift positively impacts the environment [2] (for instance, by reducing carbon emissions), it also poses new challenges in power system stability and security. Renewable resources are vulnerable to exogenous shocks, such as from weather conditions [3], resulting in increased exposure of the electricity network to power fluctuations. When combined with endogenous power disturbances due to various other system contingencies, these disturbances could in the worst case activate emergency responses in the power grid [4,5] which may propagate in a cascading fashion [6–11].

There is increasing interest in embedding battery energy storage systems (BESS) in power grids [12] to improve grid stability and resilience to disturbances [13–18] by virtue of their rapid response [19]. In this study we employ the skipping sampler, a Markov Chain Monte Carlo (MCMC) rare-event sampler, to examine the benefits of BESS as both the battery maximum power output (MPO) and the distribution of power disturbances vary. Taking a probabilistic model for the potential power disturbances at all buses (interpreted as both exogenous and endogenous), we build conditional distributions of the combinations of disturbances which lead to rare instabilities of two kinds. Firstly, to examine the frequency regulation benefits of BESS we study frequency excursions beyond the normal operating band. Then, to explore the emergency response provided by BESS, we condition on a load shedding event. Potential saturation in the benefits of BESS is examined as MPO increases, and also potential interactions between the frequency regulation and contingency services which they provide.

In this line of research we aim to combine time-domain simulation with random sampling, in order to study rare events occurring in power systems. The main challenges are that standard Monte Carlo simulation methods are unreliable in rare event settings [20], a problem compounded by the heavy computational expense of time-domain, simulation-based assessment of power system robustness [21]. In the face of these challenges, one approach is to apply carefully reformulated methods for random sampling (see for example [22]), while another is to explore alternatives to random sampling, such as those studied in [21,23,24]. However, these methods typically involve simplifying assumptions of varying strength, which may make these studies challenging to transfer to other related contexts.

This paper continues recent work based on Markov Chain Monte Carlo (MCMC) random sampling which was begun in [25,26]. While the latter papers also made strong simplifications, our goal in the present work is to demonstrate the incorporation of a power system model which is both detailed and adaptable. That is, the model and case study below incorporate network topology and nodal frequencies, third-order dynamics, automatic voltage regulation, primary and secondary frequency control, battery storage, frequency-based load and generation shedding, and rate of change of frequency (RoCoF) generator protection. We also emphasise that, as in the latter papers, any probability density may be taken as the model of power disturbances.

In [25] a simpler MCMC rare-event sampler was used to build conditional distributions of random disturbances leading to excessive RoCoF at any bus. One limitation in that work was the use of dynamics which neglect system voltage transients and are valid only for small disturbances. In order to study cascades of emergency responses caused by larger disturbances, [26] employed third-order dynamics. The latter work established the effect of network connectivity on the conditional distribution of cascade sizes (that is, the number of emergency responses arising from the initial disturbances), namely that these distributions can be highly bimodal in more highly connected networks. However, these findings were obtained through the use of toy power system models at the extremes of connectivity, namely the ring and fully connected networks. In contrast, we perform a case study based on Kundur's two-area system [27], including the additional features of BESS, line disconnection and automatic voltage

regulation. This enables study of the benefits of BESS for system robustness and resilience under uncertainty, taking into account potential interactions with emergency protection schemes.

In the spirit of the present theme issue of *Philosophical Transactions A*, we aim as far as possible for a self-contained presentation suitable for an interdisciplinary audience, with further technical detail provided in an online supplement. The results may be reproduced using the code available at `https://github.com/ahw493/`.

2. Simulation model

Our simulation model is cyber-physical, in the sense that we model physical observables (the physical layer) in continuous time while simultaneously modelling emergency protection schemes (the cyber layer) in discrete time. Between interventions from the cyber layer, the physical layer evolves via the differential equations (2.3) and (2.4). The cyber layer, which consists of the emergency protection schemes described in the supplementary material, inspects the physical layer at regular intervals. On this discrete-time lattice, if any activation criterion is met then the corresponding protection system activates. Each activation creates a discontinuity in the physical layer, resulting either from an instantaneous reduction in generation or load, or an instantaneous change to the graph topology through the loss of an edge (line).

Table 1 collects notation used in the paper. Constant and time-evolving variables are indicated using Latin and Greek letters, respectively. Lower-case Greek letters correspond to physical observables (rotor angles, frequencies, powers and voltages), while upper-case Greek letters are used to denote the state of the emergency response schemes. Vectors are underlined e.g $\underline{v}$.

(a) Network model

Consider an undirected graph $G(N+L, W)$, where $N+L$ is the set of nodes and W a set of weighted edges. The set of nodes $1, \dots, N$ represents generator buses, while the remaining $N+1, \dots, N+L$ nodes represent load buses. Edges represent power lines, and the weight W_{ij} of line ij (that is, the line between buses i and j) is the triple of characteristics $W_{ij} = (p_{ij}, e_{ij}, l_{ij})$, where p_{ij} is the reactance per unit, e_{ij} the resistance per unit and l_{ij} the length of line ij. The line indicator variable Ω_{ij} switches from 1 to 0 upon disconnection of line ij by the protection scheme. The system's susceptance matrix can then be written as a Laplacian-like matrix (see [28]), expressed in turn as a function $B(\Omega)$ of the line indicator variables:

$$B_{ij}(\Omega) \coloneqq \begin{cases} \left(\sum_{k=1}^{N+L} w_{ik}(\Omega_{ik}) \right) - w_{ij}(\Omega_{ij}) & \text{if } i = j, \\ -w_{ij}(\Omega_{ij}) & \text{if } i \neq j, \end{cases} \tag{2.1}$$

where

$$w_{ij}(\Omega_{ij}) \coloneqq \begin{cases} 0 & \text{if } i = j \\ -\dfrac{p_{ij}}{e_{ij}^2 + p_{ij}^2} \dfrac{\Omega_{ij}}{l_{ij}} & \text{if } i \neq j. \end{cases} \tag{2.2}$$

The network is assumed to be lossless, so that the susceptance matrix coincides with the imaginary part of the admittance matrix [27,29].

Table 1. Summary of notation. Note: per unit quantities are denoted p.u.

Sym.	Meaning	Units
	Equivalent generator and line parameters	
A_i	Governor droop response	MW/rad
B_{ij}	Susceptance matrix	p.u
D	Load damping factor	%
δ_i	Voltage angle	rad
$\dot{\delta}_i$	Frequency	p.u
$\ddot{\delta}_i$	Rate of change of frequency (RoCoF)	p.u
E_i	Rotor field voltage	p.u
ϵ_i^e	Automatic voltage regulation	p.u
η_i	Random power injection or drain	p.u
L_i	Equivalent machine reactance (see Supplementary Material)	ohms
$M(\underline{\Xi})$	System angular momentum	Ws^2
M_i	Generator angular momentum	Ws^2
ν_i	Voltage	p.u
P_i^m	Maximum power output	p.u
P_i^N	Initial generator power (at t= 0)	p.u
P_i^L	Initial loads (at t= 0)	p.u
ϕ_{ij}	Power flow from bus i to j	p.u
ρ_i	Mechanical power	p.u
S_i	Transient time constant d-axis	s
$\mathcal{W}$	Governor deadband frequency range	Hz
χ_i^L	Active bus loads	p.u
	Battery parameters	
β_i	Battery power injection/drain	p.u
b_i^+	Initial battery state parameter	%
B_i^0	Initial battery power	MW
B^m	Maximum battery power	MW
B^r	Maximum battery power for regulation FCAS	MW
B^g	Battery response to global frequency	MW
B^l	Battery response to local frequency	MW
F^d	Battery deadband frequency deviation	Hz
F^n	Emergency FCAS frequency deviation	Hz
F^m	Frequency deviation associated with maximum battery power	Hz
$\mathcal{E}$	Frequency interval for local battery response	Hz
$\mathcal{R}$	Frequency interval for AGC commanded battery response	Hz
$\mathcal{D}$	Battery's deadband frequency interval	Hz
T^b	AGC signal interval	s
	Protection system parameters	
C	Load shedding increments	%
Ω_{ij}	Indicator for line protection system	-
Ξ_i	Indicator for generation shedding emergency response	-
Γ_i	Indicator for load shedding emergency response	-

(b) System dynamics

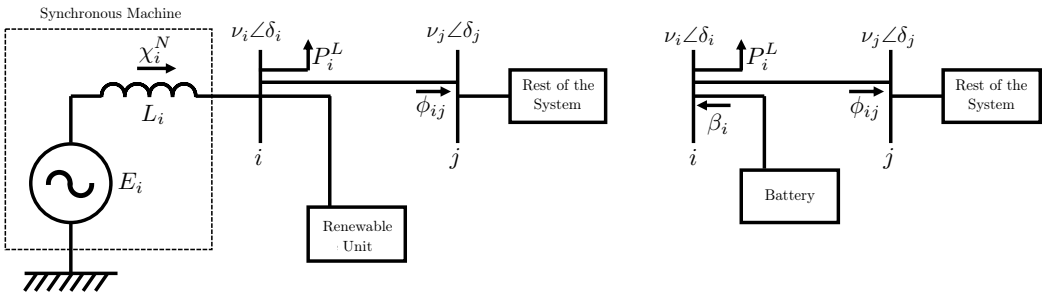

Figure 1. (Left) Generator bus including synchronous machine, local load, and renewable unit (Right) Load bus including load (modelled as a motor) and BESS. ϕ_{ij} is the power flow through the line from bus i to bus j, see Section 2.3 in the Supplementary Material. See Table 1 and main text for other notation.

Each generation bus $i = 1, \ldots, N$ includes a synchronous machine, load, and renewable unit, as shown in Figure 1 (left) and equations (2.3):

$$\begin{cases} M(\underline{\Xi})\ddot{\delta}_i + D(\underline{\Gamma})\dot{\delta}_i = \Xi_i \chi_i^N - \chi_i^L - \nu_i \sum_{j=1}^{N+L} B_{ij}(\Omega_{ij})\nu_j \sin(\delta_i - \delta_j) + \eta_i & (2.3a) \\ S_i \dot{\nu}_i = \Xi_i (E_i - \epsilon_i^e) - \nu_i + L_i \sum_{j=1}^{N+L} B_{ij}(\Omega_{ij})\nu_j \cos(\delta_i - \delta_j) & (2.3b) \\ \dot{\rho}_i = -A_i \dot{\delta}_i (1 - 1_{\mathcal{W}}[\dot{\delta}_i]) & (2.3c) \end{cases}$$

In equation (2.3*a*), $\chi_i^N := \min\{\rho_i + P_i^N, P_i^m\}$ is generator $i's$ mechanical power, P_i^N is the equilibrium mechanical power output of the generator, P_i^m is the generator's nominal maximum power output and ρ_i is the power contribution of a governor, whose dynamics are described in (2.3*c*) where $\mathcal{W}$ is the governor deadband (see Supplementary Material); voltage dynamics are given by (2.3*b*); and the terms $M(\underline{\Xi})$, $D(\underline{\Gamma})$ and ϵ_i^e are detailed below.

Each load bus $i = N+1, \ldots, N+L$ includes a load and a battery, as shown in Figure 1 (right), whose corresponding equations are

$$\begin{cases} M(\underline{\Xi})\ddot{\delta}_i + D(\underline{\Gamma})\dot{\delta}_i = -\chi_i^L + \nu_i \sum_{j=1}^{N+L} B_{ij}(\Omega_{ij})\nu_j \sin(\delta_i - \delta_j) + \beta_i & (2.4a) \\ S_i \dot{\nu}_i = E_i - \nu_i + L_i \sum_{j=1}^{N+L} B_{ij}(\Omega_{ij})\nu_j \cos(\delta_i - \delta_j). & (2.4b) \end{cases}$$

The initial conditions of the above system of equations, denoted $\delta_i(0)$, $\nu_i(0)$, $\rho_i(0)$ and P_i^N are set equal to equilibrium states which can be determined numerically. [1]

Recalling that the models of generation and load shedding are presented in the supplementary material, the variables $\underline{\Xi} := \{\Xi_1, \Xi_2, \ldots, \Xi_N\}$ are used to record activations of generation shedding emergency responses. That is, Ξ_i is initially 1 and switches to 0 when generation shedding occurs at generator node i. The global variable $M(\underline{\Xi}) := \sum_{i=1}^{N+L} \Xi_i M_i$ then represents the total angular momentum of the system, while accounting dynamically for generation shedding through its dependence on $\underline{\Xi}$. For the load buses $i = N+1, \ldots, N+L$ the values

[1] see, for example, [29] for a study of the existence of these states and Section 4 of the Supplementary Material for specific values.

$\chi_i^L := (1 - C\Gamma_i)P_i^L$ are also dynamic, due to the action of the load shedding emergency scheme. Here $0 < C < 1$ is the additional amount of load shed per activation of this emergency scheme and Γ_i counts the number of load shedding events at node i. In the same way, the global damping coefficient $D(\underline{\Gamma})$ (equation (11) in the supplementary material) accounts dynamically for load shedding events. The variable η_i representing the power disturbance at bus i is detailed in Section 3. The term ϵ_i^e accounts for the action of automatic voltage regulation (Section 1 of the supplementary material), while β_i is the battery power injection/drain defined in (2.5). Note that the sign in front of the voltage ν_i on the right-hand side of (2.4*a*) is the opposite of that in (2.3*a*), as explained by the opposite direction of the mechanical and electrical energy conversions.

(c) Battery model

Each BESS has two reference response strategies, one for response to local frequency and one for response to an Automatic Generation Control (AGC) signal based on the average global frequency. The response to local frequency takes precedence. Each of these reference strategies has a deadband region with no response, a region of linear response, and a region of fixed response. Thus the battery response is given by:

$$\beta_i := 1_{\mathcal{E}}[\dot{\delta}_i](B^l(\dot{\delta}_i) - B_i^0) + (1 - 1_{\mathcal{E}}[\dot{\delta}_i])(B^g(\dot{\underline{\delta}}) - B_i^0). \tag{2.5}$$

Here, the indicator function $1_{\mathcal{E}}[\dot{\delta}_i]$ determines whether the local frequency at bus i lies in the range $\mathcal{E} \equiv \mathcal{E}^1 \cup \mathcal{E}^2$, where $\mathcal{E}^1 \equiv (-\infty, -F^m] \cup [F^m, \infty)$ and $\mathcal{E}^2 \equiv (-F^m, -F^n] \cup [F^n, F^m)$ (see Figure 2). The terms $(B^l(\dot{\delta}_i) - B_i^0)$ and $(B^g(\dot{\underline{\delta}}) - B_i^0)$, where the functions $B^l(\delta_i))$ and $B^g(\dot{\underline{\delta}}))$ are defined below, take account of the fact that the BESS will in general be responding at a pre-contingency level B_i^0 just prior to time 0. These terms therefore model the *change* in power output when the BESS delivers its reference response. Since we do not explicitly model the state of the system prior to time 0, the values of B_i^0 are randomly sampled initial conditions, see Section 3 for more details.

(i) BESS response to local frequency δ_i

According to (2.5), if the local frequency δ_i lies in the range $\mathcal{E}$ then the BESS response is determined by this local frequency deviation. In this case the power-frequency relation of the response is given by the blue graph in Figure 2: [2]

$$B^l(\dot{\delta}_i) := \begin{cases} B^m \text{sgn}[\dot{\delta}_i] & \dot{\delta}_i \in \mathcal{E}^1 \\ \left(M^l \dot{\delta}_i + Q^l \text{sgn}[\dot{\delta}_i]\right) & \dot{\delta}_i \in \mathcal{E}^2 \\ 0 & \dot{\delta}_i \in \mathcal{R} \cup \mathcal{D} \end{cases}, \tag{2.6}$$

where $\mathcal{R} \equiv (-F^n, -F^d] \cup [F^d, F^n)$, $\mathcal{D} \equiv (-F^d, F^d)$, B^m is the battery maximum power output (MPO) and

$$M^l := \left(\frac{B^m - B^0}{F^n - F^m}\right) < 0 \text{ and } Q^l := \left|\frac{B^m F^n - B^0 F^m}{F^n - F^m}\right| \tag{2.7}$$

are respectively the slope and intercept of the diagonal blue lines in Figure 2.

(ii) BESS response to system average frequency $\dot{\underline{\delta}}$

Again from (2.5), if the local frequency δ_i lies outside the range $\mathcal{E}$ then the BESS response is determined by the system average frequency deviation through the AGC signal. In this case the

[2]The superscript l stands for "local", superscript m stands for "maximum", superscript g stands for "global", superscript r stands for "regulation".

power-frequency relation of this response is given by the red graph in Figure 2:

$$B^g(\underline{\dot{\delta}}) \coloneqq \begin{cases} B^r \mathrm{sgn}[\underline{\dot{\delta}}] & \underline{\dot{\delta}} \in \mathcal{E} \\ (M^g \underline{\dot{\delta}} + Q^g \mathrm{sgn}[\underline{\dot{\delta}}]) & \underline{\dot{\delta}} \in \mathcal{R} \\ 0 & \underline{\dot{\delta}} \in \mathcal{D} \end{cases}, \tag{2.8}$$

where

$$M^g \coloneqq \left(\frac{B^r - B^0}{F^d - F^n}\right) < 0, \text{ and } Q^g \coloneqq \left|\frac{B^r F^d - B^0 F^n}{F^d - F^n}\right| \tag{2.9}$$

are respectively the slope and intercept of the diagonal red lines in Figure 2 and the system average frequency deviation is calculated as

$$\underline{\dot{\delta}} = \underline{\dot{\delta}}(t) \coloneqq \frac{1}{N} \sum_{i=1}^{N} \dot{\delta}_i (T^b \lfloor t/T^b \rfloor). \tag{2.10}$$

The form of (2.10) takes into account time delay in the calculation, broadcast and reception of the system-wide AGC signal. The discretised time index $T^b \lfloor t/T^b \rfloor$ corresponds to reception of the AGC signal at the BESS every T^b seconds.

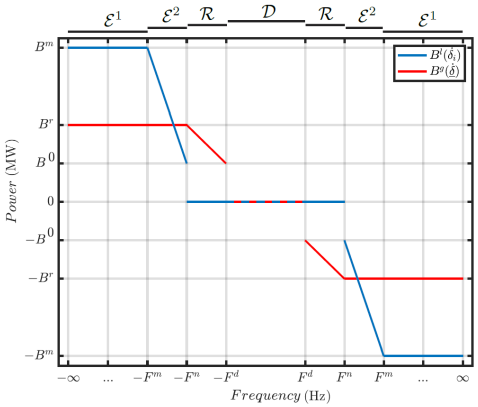

Figure 2. Reference power-frequency response strategies for the BESS response to local frequency (blue line) and the AGC signal (red line). As in (2.5), response to local frequency takes precedence. The common deadband $\mathcal{D}$ is indicated by the dashed central line.

3. Statistical Model

(a) Unconditional distribution

At each bus i we sample a random power injection or drain η_i. These random disturbances are modelled agnostically and may, for example, represent exogenous shocks and/or endogenous contingencies. They are applied as impulses at time 0 and, as in [26], are modelled as constant power disturbances over the timescale of our simulations. Thus for example, if the model is used to explore the effect of renewable generation forecast errors then the joint distribution of these disturbances should reflect the historical joint distribution of such errors, and the timescale of the simulation should be comparable to the characteristic timescale of these errors. In the case study of Section 4, to enable a straightforward parametric exploration of the effect of correlations

between disturbances, the vector $\underline{\eta}$ of disturbances is modelled as

$$\underline{\eta}(t) \coloneqq \underline{U}\Theta[t] \in \mathbb{R}^{N+L} \tag{3.1}$$

where Θ is the Heaviside step function and $\underline{U}$ is the vector of disturbance magnitudes. More generally, if it is not judged reasonable to model disturbances as static over the timescale of the simulation, then dynamic disturbances can be accounted for by augmenting the simulation model with appropriate dynamics for the disturbances η_i in equation (2.3a).

Each U_i is normalised by setting it proportional to the stationary power injection at node i. Thus $\underline{U} = \underline{u} \circ \underline{P}^0$, where $\underline{P}^0$ is the vector of equilibrium nodal power injections, $\circ$ is the component-wise product and $\underline{u} \in \mathbb{R}^{N+L}$ is taken to be a Gaussian vector

$$\underline{u} \sim \mathcal{N}(\underline{0}, \Sigma) \quad \text{where} \quad \Sigma_{ij} \coloneqq \sigma^2 \cdot \begin{cases} 1 & i = j \\ \alpha & i \neq j \end{cases} \qquad i, j \in \{1, \ldots, N+L\}, \tag{3.2}$$

with $0 \leq \alpha < 1$ to ensure positive semidefiniteness.

The pre-contingency response of the battery just prior to time 0 is sampled from a uniform distribution

$$B_i^0 \sim \mathcal{U}\left[-\frac{b^+ B^m}{2}, \frac{b^+ B^m}{2}\right] \tag{3.3}$$

(see Section 4 of the supplementary material for parameter specifications).

It is assumed that time 0 in our simulations can occur at any time in the interval between AGC signals. To reflect this, the time of the first AGC signal in the simulation is sampled uniformly:

$$T_0^b \sim \mathcal{U}[0,\ cT^b], \tag{3.4}$$

and subsequent AGC signals occur every T^b seconds.

(b) Rare event sampler

Rare event sampling is performed using the skipping sampler, a Markov Chain Monte Carlo (MCMC) algorithm developed for this purpose. The sampler belongs to the class of Metropolis-Hastings (MH) algorithms and, as proved in [30] and demonstrated in the case study of Section 4, improves performance relative to the random walk Metropolis algorithm. Starting from any state (in the present context, a vector $\underline{u}_0 \in \mathbb{R}^{N+L}$ of power disturbances), a proposed new state $\tilde{\underline{u}} \in \mathbb{R}^{N+L}$ is sampled from a so-called proposal density. The proposal $\tilde{\underline{u}}$ is either accepted or rejected according to a specified acceptance probability. If it is accepted, the proposal is added to the output sample and becomes the new state $\underline{u}_1$. This procedure is repeated a desired number of times and the output sample $\{\underline{u}_1, \underline{u}_2, \ldots\}$ is returned. The skipping sampler is dedicated to sampling from any rare event Υ of interest, since its proposal density 'skips' over the unwanted region Υ^c until the rare event Υ is sampled (or until the skipping process is halted for reasons of computational efficiency, if this occurs first).

More precisely, in rare event sampling we are given an unconditional density μ on $\mathbb{R}^{N+L}$ and a rare event $\Upsilon \subset \mathbb{R}^{N+L}$ of interest and the task is to sample from this distribution conditional on Υ. The density of this conditional distribution at the point $\underline{u} \in \mathbb{R}^{N+L}$ is

$$\pi(\underline{u}) \coloneqq \frac{\mu(\underline{u})\, \mathbf{1}_\Upsilon(\underline{u})}{\mu(\Upsilon)}, \tag{3.5}$$

where $\mu(\Upsilon)$ is the probability of the event Υ.

Pseudocode for the skipping sampler is given in Algorithm 1. Given the current state $\underline{u}$, the proposal $\tilde{\underline{u}}$ is a random walk proposal. If $\tilde{\underline{u}} \notin \Upsilon$, we calculate the direction $\underline{\Phi} = (\tilde{\underline{u}} - \underline{u}) / \|\tilde{\underline{u}} - \underline{u}\|$ between these two points, and move ('skip') a further independent random distance R_1 in this direction, where R_1 has the conditional distribution of $\|\tilde{\underline{u}} - \underline{u}\|$ when conditioned on the observed value of $\underline{\Phi}$. If the modified proposal $\underline{Z} = \underline{u} + R_1\underline{\Phi}$ lies in Υ then it is either accepted or rejected according to the acceptance probability $\alpha(\underline{u}, \underline{Z})$, otherwise the process skips again in the same

direction $\underline{\Phi}$, by an independent random distance R_2 having the same distribution as R_1, and so on, until either Υ is entered or the budget for skipping is exhausted.

We take the unconditional distribution μ to be the Gaussian distribution in (3.2) above, and let the set Υ be a particular system instability. While the underlying sampler is the same as that employed in [26], in the case study of Section 4 below the system model and simulator aim to be more realistic and we are interested in instabilities relating to two different services provided by BESS (that is, regulation and emergency responses) and their interaction.

Input : The n-th sample $\underline{u}_n$

Set $\underline{u} \coloneqq \underline{u}_n$;
Generate an initial proposal $\tilde{\underline{u}}$ distributed according to the density $q(\underline{y} - \underline{u})d\underline{y}$;
Calculate the direction $\Phi = (\tilde{\underline{u}} - \underline{u}) \,/\, \|\tilde{\underline{u}} - \underline{u}\|$;
Generate a halting index $K \sim K_\varphi$;
Set $k = 1$ and $\underline{Z}_1 \coloneqq \tilde{\underline{u}}$;
while $\underline{Z}_k \notin \Upsilon$ **and** $k < K$ **do**
  Generate a distance increment R distributed according to $q_{r|\Phi}(r|\Phi)$;
  Set $\underline{Z}_{k+1} = \underline{Z}_k + \Phi R$;
  Increase w by one;
end
Set $\underline{Z} \coloneqq \underline{Z}_k$;
Evaluate the acceptance probability:

$$\alpha(\underline{u}, \underline{Z}) = \begin{cases} \min\left(1, \frac{\pi(\underline{Z})}{\pi(\underline{u})}\right) & \text{if } \pi(\underline{u}) \neq 0, \\ 1, & \text{otherwise,} \end{cases} \tag{3.6}$$

Generate a uniform random variable V on $(0, 1)$;
if $V \leq \alpha(\underline{u}, \underline{Z})$ **then**
  $\underline{u}_{n+1} = \underline{Z}$;
else
  $\underline{u}_{n+1} = \underline{u}$;
end
return $\underline{u}_{n+1}$.

Algorithm 1: Skipping sampler (n-th step). Here q is a symmetric random walk proposal density and $q_{r|\Phi}(r|\Phi)$ is the conditional density of its polar radial coordinate r given the polar angle Φ, see [30] for full details.

4. Case Study

(a) Kundur Two-Area System

Our case study is based on the Kundur two-area system (KTAS) [27]. In particular we take a Kron reduced version (see for example [31,32]) consisting of $N = 4$ generation buses and $L = 2$ load buses as in Figure 3. For simplicity the load buses are equipped with equally specified batteries. In equilibrium, power flows from Area 1 to Area 2 through the line connecting nodes 5 and 6. This is modelled as a weak tie line (see for example [33]) with a disconnection ('line tripping') scheme. The system parameters (whose values can be found in Section 4 of the Supplementary Material) are such that the system is $N - 1$ secure, in the sense that the loss of a generator (in the absence of any other disturbance) does not trigger an emergency response.

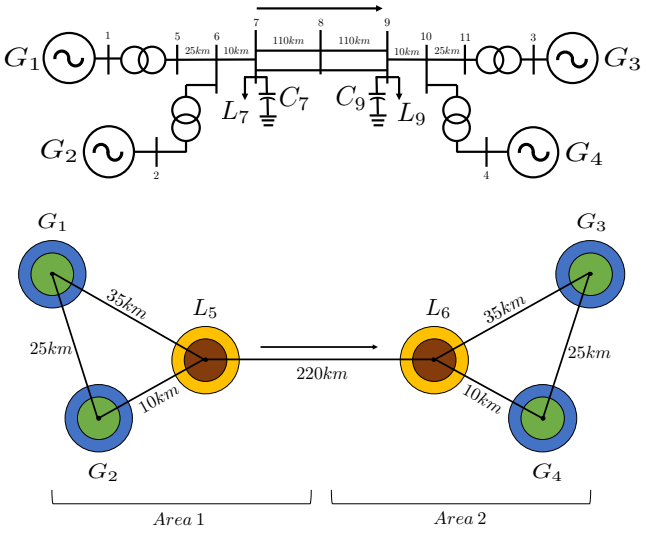

Figure 3. (Top) Single line diagram of the Kundur two-area 4 node network, reproduced from [27], before Kron reduction. (Bottom) Schematic drawing of the same system after Kron reduction. Generator buses (green circles) correspond to nodes $i = 1, \ldots, 4$ and load buses (brown circles) correspond to nodes $i = 5, 6$. Governors (blue annuli) are attached to generator buses while BESS (yellow annuli) are located at load buses. Line lengths are indicated.

(b) Metrics for instability

In order to explore the frequency regulation benefits of BESS, the first metric we apply is the frequency excursion area (FEA) which may be defined per bus as

$$\mathcal{F}_i(t) := \int_0^t \Big\{ \Theta[\dot\delta_i(s) - \mathcal{F}^+](\dot\delta_i(s) - \mathcal{F}^+)ds + \Theta[\mathcal{F}^- - \dot\delta_i(s)](\mathcal{F}^- - \dot\delta_i(s)) \Big\} ds, \tag{4.1}$$

where $\mathcal{F}^+$ and $\mathcal{F}^-$ are constant thresholds. Thus the FEA is the area lying between the graph of frequency at bus i and the frequency band $[\mathcal{F}^+, \mathcal{F}^-]$.

To measure the emergency response benefits of BESS, the metric of interest is the amount of load shed (equivalently, the numbers Γ_i of load shed events at the load buses, as defined in section 2.2 of the supplementary material). The system averages of these quantities are then

$$\mathscr{F}(t) := \frac{1}{N+L} \sum_{i=1}^{N+L} \mathcal{F}_i(t) \quad \text{and} \quad \mathscr{G}(t) := \frac{1}{L} \sum_{i=N+1}^{N+L} \Gamma_i(t) \tag{4.2}$$

In equilibrium we have $\mathscr{F}(t) = 0$ and $\mathscr{G}(t) = 0$. Recalling Section 3(b), the rare events of interest are the sets $\Upsilon^{\mathscr{F}}$ and $\Upsilon^{\mathscr{G}}$, corresponding to frequency excursions and load shedding respectively, where:

$$\Upsilon^{\mathscr{F}} := \{\underline{u} \in \mathbb{R}^{N+L} : \mathscr{F}(T) > 0\} \quad \text{and} \quad \Upsilon^{\mathscr{G}} := \{\underline{u} \in \mathbb{R}^{N+L} : \mathscr{G}(T) > 0\}. \tag{4.3}$$

Here $T > 0$ is the length of the observation time window considered. In direct analogy with the well-known conditional value at risk (CVaR) metric, we may then define the conditional average load shed as

$$\langle \mathscr{G}(T) \rangle := \sum_{i=1}^{L\Delta} \mathscr{G}(T) \cdot \mathbb{P}[\mathscr{G}(T) = i | \Upsilon^{\mathscr{G}}], \tag{4.4}$$

where Δ is the maximum possible number of load shed events per node (see Section 2.2 in the supplementary material). Thus $\langle \mathscr{G}(T) \rangle$ measures the severity of load shedding, given that it occurs. We may similarly define the conditional average FEA $\langle \mathscr{F}(T) \rangle$, measuring the severity of

frequency excursions when they occur. The conditional samples output by the skipping sampler of Section 3(b) may be used to calculate the simulation values of these conditional metrics.

(c) Skipping sampler implementation

In Algorithm 1, the halting index is taken to be constant and the proposal q to be Gaussian, so that the conditional distribution $q_{r|\varphi}$ of the polar radial coordinate r of the initial proposal is the generalised Gamma distribution

$$q_{r|\varphi}(r|\varphi) = \frac{(\varphi^T \Sigma^{-1} \varphi)^{\frac{N+L}{2}}}{2^{\frac{N+L}{2}-1}\Gamma(\frac{N+L}{2})} e^{-(\varphi^T \Sigma^{-1}\varphi)\frac{r^2}{2}} r^{N+L-1}. \tag{4.5}$$

5. Results

In this section we explore how the frequency regulation and emergency response benefits of BESS vary with both the BESS Maximum Power Output (MPO) B^m and the correlation parameter α for disturbances. Based on BESS characteristics anticipated in the near future [34] we take B^m from 0 (no BESS) to $1000MW$ (the maximum BESS MPO considered). Simulations were conducted using MATLAB®, each taking between 2 and 5 seconds to execute for a given vector of initial conditions using a desktop machine. To compare the computational complexity of the skipping sampler to standard Metropolis-Hastings and Monte Carlo sampling, in the study of Section (a) with 1GW battery, independent 15 minute runs generated 112, 63, and 9 samples from the skipping sampler, MH, and Monte Carlo samplers respectively. In the study of Section (b) with 1GW battery, independent 15 minute runs generated 95, 53 and 3 samples from the skipping sampler, MH, and Monte Carlo samplers respectively.

(a) Frequency regulation benefits of BESS

Figure 4 (Left) illustrates the relationship between battery MPO and $\langle \mathscr{F}(T) \rangle$, the conditional average frequency excursion area, for different values of α. The results reveal a clear decreasing trend in $\langle \mathscr{F}(T) \rangle$, approximately in the interval $[0, 400]$ MW for MPO, while the frequency regulation benefit tends to saturate beyond this level.

Figure 4 (Centre) plots the conditional average magnitude of disturbances in the rare set $\Upsilon^{\mathscr{F}}$, showing an increasing trend. Recalling the 'bell-shaped curve' of the Gaussian distribution, this indicates that the event $\Upsilon^{\mathscr{F}}$ becomes increasingly rare as battery MPO increases. Thus higher MPOs correspond to a reduction in both the likelihood of frequency excursions outside the normal operating band and, when they occur, the frequency excursions are less severe on average. While this reduction in severity saturates as MPO increases to 1GW, the reduction in frequency appears to be maintained up to this level.

These measures of severity and likelihood may be combined to produce a normalised version of conditional Average FEA, calculated by dividing $\langle \mathscr{F}(T) \rangle$ by the average magnitude of disturbances in the set $\Upsilon^{\mathscr{F}}$. This quantity is illustrated in Figure 4 (Right). Although this shows the same trend as Figure 4 (Left) in the present case of FEA, it is of greater interest in the next section.

(b) Emergency response benefits of BESS

Figure 5 replicates the plots introduced in Figure 4, this time for the conditional average load shed metric. Recalling the above discussion of Figure 4, the relationships are more complex when we consider load shedding, a rarer instability. In the left panel, the conditional average load shed is initially approximately constant as MPO increases, after which a significant decreasing relationship is seen. From the centre panel, the conditional average disturbance size initially increases, after which a significant decrease is observed. Together this implies that as MPO increases from 0 to 1GW, the initial benefit of BESS is in reducing the likelihood of load shedding

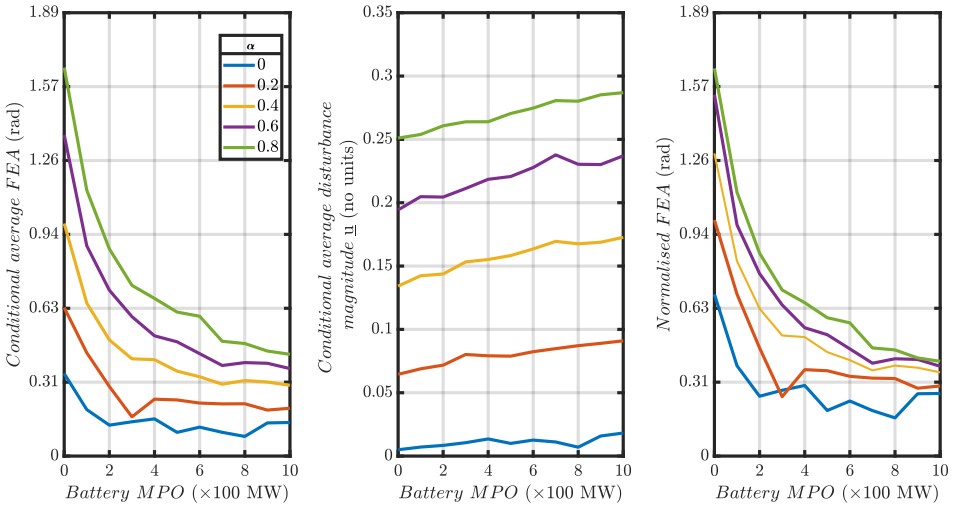

Figure 4. Conditioned on the rare event $\Upsilon^{\mathscr{F}}$ (occurrence of a frequency excursion outside normal operating band), the above plots illustrate (Left): Plot of the conditional average FEA; (Centre): Plot of conditional average disturbance magnitude against battery MPO; (Right): Plot of normalised FEA versus battery MPO.

while its severity remains approximately constant. After this initial trend, significant reductions in severity are balanced against significant increases in the likelihood of load shedding (as evidenced by the decrease in conditional average disturbance size). When these two aspects are weighed against each other in the right panel through normalisation, a consistent improvement in system resilience under this metric is observed with increasing MPO, with the exception of the cases of highest correlation between disturbances ($\alpha = 0.6, 0.8$).

Figure 6 investigates further the phenomena observed in Figure 5. As shown in the left panel, the increase in normalised load shedding seen for $\alpha = 0.6, 0.8$ coincides with an increase in disconnection of the weak tie line between nodes 5 and 6. Further investigation (data not shown) reveals that in this parameter range, load shedding was associated with the occurrence of large negative disturbances in Area 2 of the KTAS. A plausible explanation is that with this combination of parameters and disturbances, the BESS in Area 1 contributes to excessive power transfer to Area 2, resulting in disconnection of the weak tie line. The additional transient dynamics resulting from the consequent system separation exacerbate the on-going cascade of both load shedding and generation shedding (right panel), reducing system resilience. Additionally, the centre panel of Figure 5 reveals a different but similarly complex relationship between MPO and the probability of generation shedding due to RoCoF.

(c) Interaction between frequency regulation and contingency services

Recall from Section 3 that to account for the frequency regulation service provided by BESS, the power injection or withdrawal B_i^0 from each battery just before time 0 is sampled from a uniform distribution. Also, from equation (2.5), this initial state determines the maximum power available to respond to the disturbances at time 0. To confirm that the model captures interaction of the frequency regulation and emergency responses, the top row of Figure 7 plots the full distribution of B_i^0 at the two buses with BESS ($i = 5, 6$), when conditioned on $\Upsilon^{\mathscr{G}}$ (that is, conditioned on load shedding). The top left pair plots results for MPO 200MW, and from visual inspection the conditional distribution is again approximately uniform. In contrast the top right pair of distributions, which plots results for MPO 1GW, are markedly skewed. This indicates interaction between the frequency regulation and contingency services, since load shedding is associated

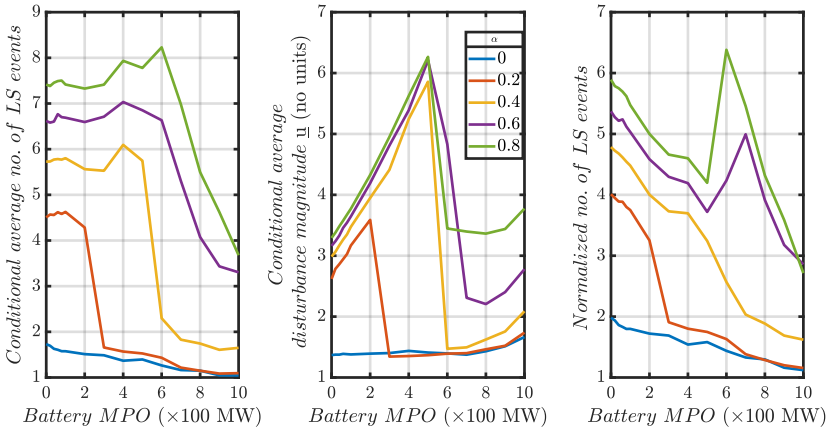

Figure 5. Conditioned on the rare event $\mathcal{T}^{\mathcal{G}}$ (occurrence of at least one load shed event), the above plots illustrate (Left): Plot of the conditional average load shed; (Centre): Plot of conditional average disturbance magnitude against battery MPO; (Right): Plot of normalised load shed versus battery MPO.

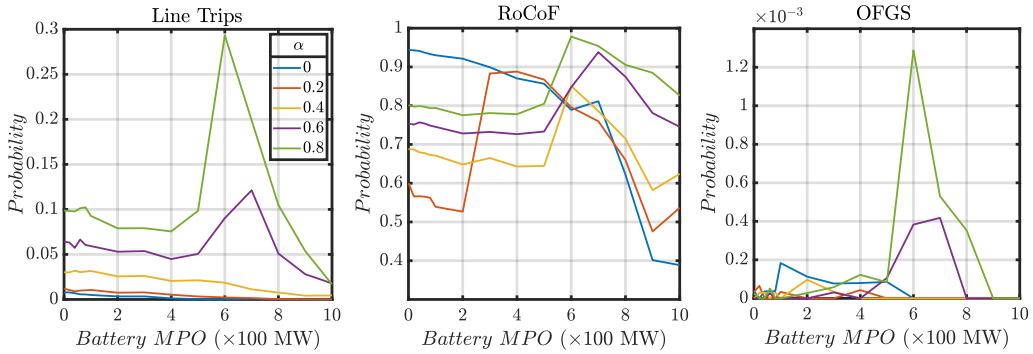

Figure 6. Conditioned on the rare event $\mathcal{T}^{\mathcal{G}}$ (occurrence of at least one load shed event), the above plots illustrate (Left): Conditional probability of line trip; (Centre): Conditional probability of generation shedding due to rate of change of frequency; (Right) Conditional probability of over frequency generation shedding.

with high values of B_5^0 (the initial BESS power in Area 1) and low values of B_6^0 (the initial BESS power in Area 2).

Indeed the bottom left panel shows that, for MPO 1GW, the conditional average disturbance at node 5 is positive, while it is negative at node 6. Thus in this case study, load shedding is associated with disturbances which are in the same direction and thus reinforce the initial power outputs B_i^0 $(i = 5, 6)$, rather than being in the opposite direction and thus partially cancelling them. The bottom right panel confirms that this potential issue may be mitigated by judicious choice of the parameter b^+ in (3.3): taking MPO 1GW and $b^+ = 0.2$, the conditional distribution of B_i^0 is markedly less skewed.

6. Conclusions and outlook

Our results demonstrate successful application of rare event sampling to a detailed power system dynamic simulation model including BESS. The method accounts for the feedback

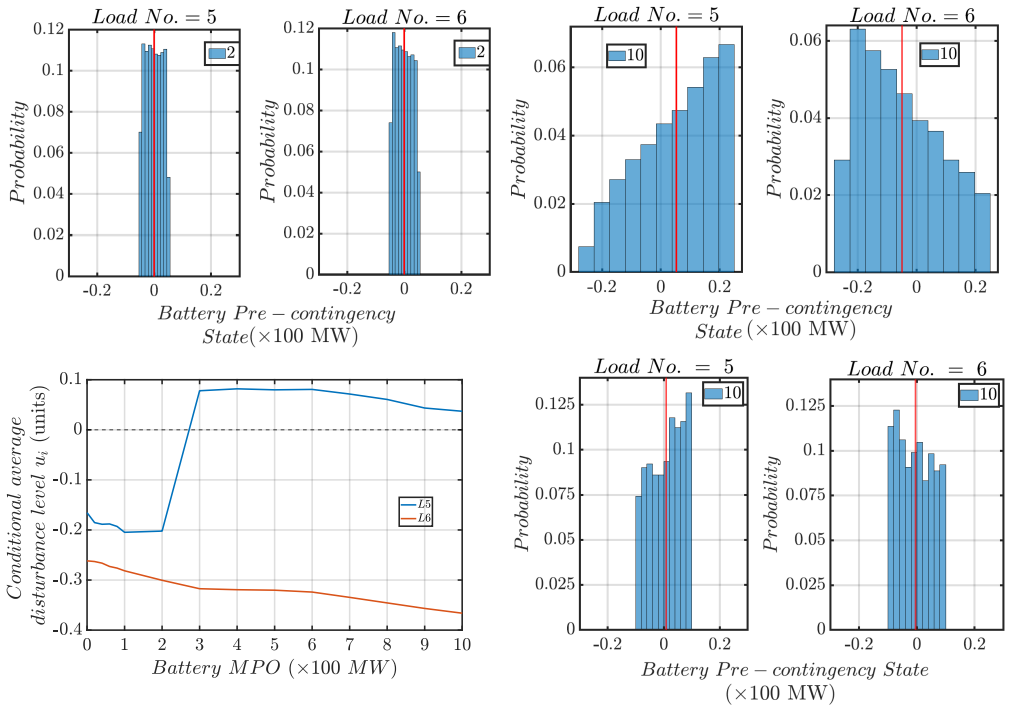

Figure 7. Empirical distributions of the BESS initial output power B_i^0 for $i = 5, 6$, conditional on the event $\mathcal{Y}^{\mathcal{G}}$ (that is, conditional on load shedding), for $\sigma^2 = 0.003$ and $\alpha = 0.2$. Vertical red lines locate the conditional mean. (Top Left Pair): MPO 200 MW, $b^+ = 1$. (Top Right Pair): MPO 1GW, $b^+ = 1$. (Bottom Right Pair): MPO 1GW, $b^+ = 0.2$. (Bottom Left): Plot of the conditional average disturbance level (including sign) at buses 5 and 6 versus battery MPO.

effects of emergency responses and is flexible, producing a wide variety of empirical statistics capable of distinguishing between the likelihood and severity of instabilities, and of identifying both saturation in these benefits as MPO increases and competition between the frequency regulation and emergency responses provided by BESS. Possible future research directions include extensions to further protection systems such as voltage regulation, more detailed sensitivity analyses including the influence of BESS speed of response, and investigation of the effect of different network topologies.

Authors' Contributions. MG produced the code for the simulations, while both MG and AP conducted simulated experiments. MG, JM and AP and analysed the results and drafted the manuscript. All authors read and approved the manuscript.

Competing Interests. The authors declare that they have no competing interests.

Funding. AP and JM acknowledge support from EPSRC grant EP/P002625/1 and the Alan Turing Institute (Lloyd's Register Foundation and Data-Centric Engineering Programme). MG acknowledges support from the Queen Mary, University of London Principal's Studentship for Post-Graduate Research. The authors would like to thank the Isaac Newton Institute for Mathematical Sciences for support and hospitality during the programme The Mathematics of Energy Systems, when work on this paper was undertaken supported by EPSRC grant number EP/R014604/1.

Acknowledgements. We are grateful for several insightful discussions with Pierluigi Mancarella and Mehdi Ghazavi Dozein regarding case study design and details of the simulation model.

References

1. International Renewable Energy Agency.

Global Energy Transformation: A roadmap to 2050.
2018.

2. Dolf Gielen, Francisco Boshell, Deger Saygin, Morgan D Bazilian, Nicholas Wagner, and Ricardo Gorini.
The role of renewable energy in the global energy transformation.
Energy Strategy Reviews, 24:38–50, 2019.
3. Mathaios Panteli and Pierluigi Mancarella.
Influence of extreme weather and climate change on the resilience of power systems: Impacts and possible mitigation strategies.
Electric Power Systems Research, 127:259–270, 2015.
4. Ahvand Jalali, Mehdi Ghazavi Dozein, and Pierluigi Mancarella.
Frequency stability provision from battery energy storage system considering cascading failure s with applications to separation events in Australia.
In *2019 IEEE Milan PowerTech*, pages 1–6. IEEE, 2019.
5. Mehdi Ghazavi Dozein and Pierluigi Mancarella.
Possible negative interactions between fast frequency response from utility-scale battery storage and interconnector protection schemes.
In *2019 29th Australasian Universities Power Engineering Conference (AUPEC)*, pages 1–6. IEEE, 2019.
6. Paul Hines, Karthikeyan Balasubramaniam, and Eduardo Cotilla Sanchez.
Cascading failures in power grids.
IEEE Potentials, 28(5):24–30, 2009.
7. A Muir and J Lopatto.
Final report on the august 14, 2003 blackout in the United States and Canada: causes and recommendations, 2004.
8. Göran Andersson, Peter Donalek, Richard Farmer, Nikos Hatziargyriou, Innocent Kamwa, Prabhashankar Kundur, Nelson Martins, John Paserba, Pouyan Pourbeik, Juan Sanchez-Gasca, et al.
Causes of the 2003 major grid blackouts in north America and Europe, and recommended means to improve system dynamic performance.
IEEE transactions on Power Systems, 20(4):1922–1928, 2005.
9. Vaishali Rampurkar, Polgani Pentayya, Harivittal A Mangalvedekar, and Faruk Kazi.
Cascading failure analysis for Indian power grid.
IEEE Transactions on Smart Grid, 7(4):1951–1960, 2016.
10. Defense Use Case.
Analysis of the cyber attack on the Ukrainian power grid.
Electricity Information Sharing and Analysis Center (E-ISAC), 2016.
11. Ruifeng Yan, Tapan Kumar Saha, Feifei Bai, Huajie Gu, et al.
The anatomy of the 2016 South Australia blackout: A catastrophic event in a high renewable network.
IEEE Transactions on Power Systems, 33(5):5374–5388, 2018.
12. Alexdandre Oudalov, Daniel Chartouni, Christian Ohler, and G Linhofer.
Value analysis of battery energy storage applications in power systems.
In *2006 IEEE PES Power Systems Conference and Exposition*, pages 2206–2211. IEEE, 2006.
13. Yutian Zhou, Mathaios Panteli, Rodrigo Moreno, and Pierluigi Mancarella.
System-level assessment of reliability and resilience provision from microgrids.
Applied Energy, 230:374–392, 2018.
14. Rodrigo Moreno, Alexandre Street, José M Arroyo, and Pierluigi Mancarella.
Planning low-carbon electricity systems under uncertainty considering operational flexibility and smart grid technologies.
Philosophical Transactions of the Royal Society A: Mathematical, Physical and Engineering Sciences, 375(2100):20160305, 2017.
15. Mohammed Benidris, Salem Elsaiah, Samer Sulaeman, and Joydeep Mitra.
Transient stability of distributed generators in the presence of energy storage devices.
In *2012 North American Power Symposium (NAPS)*, pages 1–6. IEEE, 2012.
16. Elyas Rakhshani and Pedro Rodriguez.
Inertia emulation in AC/DC interconnected power systems using derivative technique considering frequency measurement effects.

IEEE Transactions on Power Systems, 32(5):3338–3351, 2016.

17. Mehdi Ghazavi Dozein and Pierluigi Mancarella.
Application of utility-connected battery energy storage system for integrated dynamic services.
In *2019 IEEE Milan PowerTech*, pages 1–6. IEEE, 2019.
18. Pascal Mercier, Rachid Cherkaoui, and Alexandre Oudalov.
Optimizing a battery energy storage system for frequency control application in an isolated power system.
IEEE Transactions on Power Systems, 24(3):1469–1477, 2009.
19. Nemica Kadel, Wei Sun, and Qun Zhou.
On battery storage system for load pickup in power system restoration.
In *2014 IEEE PES General Meeting | Conference & Exposition*, pages 1–5. IEEE, 2014.
20. Brendan Patch and Bert Zwart.
Analyzing large frequency disruptions in power systems using large deviations theory.
In *Probabilistic Methods Applied to Power Systems (PMAPS) 2020*, 2020.
21. Dongchan Lee, Liviu Aolaritei, Thanh Long Vu, and Konstantin Turitsyn.
Robustness against disturbances in power systems under frequency constraints.
IEEE Transactions on Control of Network Systems, 6(3):971–979, 2019.
22. Art B Owen, Yury Maximov, Michael Chertkov, et al.
Importance sampling the union of rare events with an application to power systems analysis.
Electronic Journal of Statistics, 13(1):231–254, 2019.
23. Tommaso Nesti, Alessandro Zocca, and Bert Zwart.
Emergent failures and cascades in power grids: a statistical physics perspective.
Physical review letters, 120(25):258301, 2018.
24. Michael Chertkov, Feng Pan, and Mikhail G Stepanov.
Predicting failures in power grids: The case of static overloads.
IEEE Transactions on Smart Grid, 2(1):162–172, 2010.
25. John Moriarty, Jure Vogrinc, and Alessandro Zocca.
Frequency violations from random disturbances: an MCMC approach.
In *2018 IEEE Conference on Decision and Control (CDC)*, pages 1598–1603. IEEE, 2018.
26. Moriarty John Goodridge, Maldon and Andrea Pizzoferrato.
Distributions of cascade sizes in power system emergency response.
In *Probabilistic Methods Applied to Power Systems (PMAPS) 2020*, 2020.
27. Prabha Kundur, Neal J Balu, and Mark G Lauby.
Power system stability and control, volume 7.
McGraw-hill New York, 1994.
28. Mihai Cucuringu, Andrea Pizzoferrato, and Yves van Gennip.
An mbo scheme for clustering and semi-supervised clustering of signed networks.
2019.
29. Katrin Schmietendorf, Joachim Peinke, Rudolf Friedrich, and Oliver Kamps.
Self-organized synchronization and voltage stability in networks of synchronous machines.
The European Physical Journal Special Topics, 223(12):2577–2592, 2014.
30. John Moriarty, Jure Vogrinc, and Alessandro Zocca.
The skipping sampler: A new approach to sample from complex conditional densities.
arXiv preprint arXiv:1905.09964, 2019.
31. Florian Dorfler and Francesco Bullo.
Kron reduction of graphs with applications to electrical networks.
IEEE Transactions on Circuits and Systems I: Regular Papers, 60(1):150–163, 2012.
32. Florian Dorfler and Francesco Bullo.
Synchronization of power networks: Network reduction and effective resistance.
IFAC Proceedings Volumes, 43(19):197–202, 2010.
33. Sebastián Püschel-Løvengreen, Mehdi Ghazavi Dozein, Steven Low, and Pierluigi Mancarella.
Separation event-constrained optimal power flow to enhance resilience in low-inertia power systems.
Electric Power Systems Research, 189:106678, 2020.
34. Battery Storage in the United States : An Update on Market Trends.
Technical Report July, United States Energy Information Administration, Washington D.C, 2020.